



# Impaired Glymphatic Transport Kinetics Following Induced Acute Ischemic Brain Edema in a Mouse pMCAO Model

Jianying Zhang<sup>1</sup>, Hongchen Zhao<sup>1</sup>, Yang Xue<sup>1</sup>, Yiqi Liu<sup>1</sup>, Guohang Fan<sup>1</sup>, He Wang<sup>2\*</sup>, Qiang Dong<sup>1,3,4\*</sup> and Wenjie Cao<sup>1\*</sup>

<sup>1</sup> Department of Neurology, Huashan Hospital, Fudan University, Shanghai, China, <sup>2</sup> The Key Laboratory of Computational Neuroscience and Brain-Inspired Intelligence, Institute of Science and Technology for Brain-Inspired Intelligence, Fudan University, Shanghai, China, <sup>3</sup> State Key Laboratory of Medical Neurobiology, Fudan University, Shanghai, China, <sup>4</sup> National Clinical Research Center for Aging and Medicine, Huashan Hospital, Fudan University, Shanghai, China

## OPEN ACCESS

### Edited by:

Sheng Zhang,  
Zhejiang Provincial People's  
Hospital, China

### Reviewed by:

Xiaoming Rong,  
Sun Yat-sen University, China  
Mootaz M. Salman,  
University of Oxford, United Kingdom

### \*Correspondence:

He Wang  
hewang@fudan.edu.cn  
Qiang Dong  
dongqiang2222@gmail.com  
Wenjie Cao  
wenjiecao@fudan.edu.cn

### Specialty section:

This article was submitted to  
Applied Neuroimaging,  
a section of the journal  
Frontiers in Neurology

**Received:** 22 January 2022

**Accepted:** 18 February 2022

**Published:** 17 March 2022

### Citation:

Zhang J, Zhao H, Xue Y, Liu Y, Fan G,  
Wang H, Dong Q and Cao W (2022)  
Impaired Glymphatic Transport  
Kinetics Following Induced Acute  
Ischemic Brain Edema in a Mouse  
pMCAO Model.  
Front. Neurol. 13:860255.  
doi: 10.3389/fneur.2022.860255

**Background:** Cerebral edema forms immediately after blood flow interruption in ischemic stroke, which largely increased the death and disability. The glymphatic (glial-lymphatic) pathway is a major regulator of the brain liquid dynamics and homeostasis. This study aimed to investigate the transport kinetics of the glymphatic system after the appearance of ischemic edema.

**Methods:** In this study, a coated filament was attached to the left middle cerebral artery (MCA) of mice to establish a mouse model of permanent middle cerebral artery occlusion with an intact blood-brain barrier (BBB). The glymphatic function was then quantified using contrast-enhanced MRI (11.7T) by employing an injection of gadobenate dimeglumine (BOPTA-Gd) into the cisterna magna of mice. We then evaluated the expression and polarization of aquaporin-4 (AQP4) as a proxy for the physiological state of the glymphatic system.

**Results:** Our results revealed a positive correlation between the signal intensity in T1-weighted images and the corresponding apparent diffusion coefficient (ADC) values in the cortex, striatum, and periventricular zone, suggesting that impaired glymphatic transport kinetics in these regions is correlated to the cytotoxic edema induced by the occlusion of MCA. Furthermore, the increased depolarization of AQP4 in the parenchyma perivascular space (PVS) was consistent with glymphatic failure following the induced early cerebral ischemic edema.

**Conclusions:** Glymphatic transport kinetics were suppressed between the onset of cytotoxic edema and the disruption of the BBB, which correlated with the diminishing ADC values that vary based on edema progression, and is associated with depolarization of AQP4 in the parenchyma PVSs.

**Keywords:** magnetic resonance imaging, glymphatic, aquaporin-4, cerebral ischemic edema, polarization

## INTRODUCTION

The severity of cerebral edema following ischemic stroke is predictive of a patient's functional outcome (1). However, current treatment options are often ineffective. Ischemic cerebral edema occurs soon after the cerebral blood flow (CBF) interruption, which can lead to severe stroke-related damage (2). This phenomenon is further exacerbated if the edema is aggravated and can lead to long-term or permanent effects even after the vessels are successfully re-canalized. In patients with early postischemia neurological deterioration, the effect of cerebral edema on the clinical outcome of reperfusion therapy is generally more pronounced (3). Cerebral edema after stroke has mainly been thought to be caused by the destruction of the blood-brain barrier (BBB) (4), which can allow blood components to penetrate this boundary, enter the parenchyma, and damage the tissue. Because of this, previous studies investigating the mechanism of cerebral edema have largely focused on the destruction of the BBB (5). Nevertheless, recent reports showed that cerebral edema develops several hours before significant dysfunction of the BBB (6), which posed a new question regarding other influential factors that arise cerebral ischemia edema. In fact, cytotoxic edema begins within minutes of ischemic destruction and is triggered by spreading depolarizations (SDs). These traveling neurophysiological events form a dysregulated ion homeostasis that often results in cell swelling (7), and are often accompanied by ionic edema and the net entry of water and ions into the brain (8), defined as interstitial edema. Based on this series of evidence, there exists a key time window between the onset of cytotoxic edema and the disruption of the BBB in which the transformation of cytotoxic edema to vasogenic edema occurs.

A previous study verified that an increased glymphatic influx of cerebrospinal fluid (CSF) into the parenchyma perivascular spaces (PVSs) (9) of ischemic brain tissue might be the actual cause of supracute ischemic brain edema (10). CSF influx was observed at ( $11.4 \pm 1.8$  s) and ( $5.24 \pm 0.48$  min), and was driven by SDs in the cortex following cerebral ischemia and led to edema (10). We then asked in a follow-up study how the kinetics of glymphatic functions were affected after the influx of the CSF. This influx occurred through the glymphatic system which is a brain-wide mass clearance system (11) that functions through fluid transport and has been confirmed in both humans (12) and mice (9, 13). In particular, the PVSs by which the CSF and interstitial fluid (ISF) exchange occurs act as flow channels that ensheath the cerebral vasculature in the mammalian brain (9). Aquaporin-4 (AQP4) is an essential water channel protein that facilitates this process through a complex network of astrocytes (14) that are localized throughout brain tissues facing the PVS (15) and ventricle lining (16). The glymphatic system, therefore, supports convective bulk flow (9, 14) by astrocytic paracellular fluid transport and facilitates the drainage of brain ISF between para-arterial influx and paravenular efflux. We hypothesize this process may facilitate brain swelling by glymphatic malfunctions.

In this study, we aimed to explore the alteration in glymphatic dynamics after the accumulation of fluid in

the brain parenchyma and periventricular zone. We also assessed glymphatic system dysfunction and its correlation with parenchymal and periventricular edema based on the signal intensity (SI) in T1-weighted images (T1WIs) and the corresponding apparent diffusion coefficient (ADC) value and further explored the altered polarization patterns of AQP4 in various affected edema regions in permanent middle cerebral artery occlusion (pMCAO) mice. We quantified the kinetics of glymphatic drainage using 11.7T contrast-enhanced magnetic resonance imaging (CEMRI) with intracisternal injections of BOPTA-Gd (17) after the onset of ischemic edema in a mouse model of pMCAO without BBB disruption (18). The glymphatic functions of sham-operated and pMCAO mice were characterized along both spatial and temporal features to identify glymphatic malfunction in the edema mouse brain induced by occlusion of the MCA.

## MATERIALS AND METHODS

The data that support the findings of this study are available from the corresponding author upon reasonable request and are subject to institutional agreements and ethical approvals. All experiments were reported in compliance with the ARRIVE guidelines 2.0 (ARRIVE, Animal Research: Reporting *in Vivo* Experiments) (19).

### Animals

All animal procedures were approved by the Huashan Hospital Institutional Review Board. The reason for using only male mice is that estrogen has been shown to significantly affect ischemic stroke (20). Male C57/BL6 mice (bodyweight 25–30 g) aged 10–12 weeks old were used in this study. Animals were housed at constant temperature ( $25^{\circ}\text{C} \pm 2^{\circ}\text{C}$ ) with a 12/12 h light/dark cycle and were provided with *ad libitum* access to food and water. Animals were randomly assigned to two groups using excel-generated random numbers: the sham-operated group or the pMCAO group. The experimenters were blinded to pretreatments and data analysis. This study was carried out per the recommendations of the National Science Council of the Republic of China. All efforts were made to minimize animal suffering and the number of experimental animals used.

### pMCAO Model

Previous studies investigating the mechanism of cerebral ischemic edema have mainly focused on the destruction of BBB (5). To do this, most experiments used an animal model of cerebral ischemia/reperfusion. By contrast, the BBB remains intact during permanent MCA occlusion (18), as indicated by continuous isolectin-B4 (IB4) staining (21), which allows for the mechanistic study of ischemic brain edema with an intact BBB. To perform pMCAO, mice were initially anesthetized with 4% isoflurane in 1 l/min oxygen delivered through a nose cone. The isoflurane was then adjusted to between 1.5 and 3% in 1 l/min oxygen to maintain anesthesia and normal breathing throughout the procedure. Animal body temperature was maintained at  $37^{\circ}\text{C}$  with a heating pad throughout the procedure. A laser

Doppler probe was fixed on the skull 5 mm lateral to and 2 mm posterior to Bregma. A coated filament (1622A4, Cinontech Co. Ltd., Beijing, China) was then placed at the left MCA under a stereomicroscope. Concurrent CBF recordings were recorded by laser Doppler to ensure that it was below 25% of baseline. Only the mice presenting with MCAO on a 3D (three-dimensional)-TOF (time-of-flight) MRI performed immediately after surgery were included in subsequent analyses.

### Intracisternal Perfusion of Gadolinium-Based Contrast Agents

About 4  $\mu$ l of BOPTA-Gd was injected into the cisterna magna with a microsyringe pump (ALC-IP600(H), ALCOTT, Shanghai, China) and a pulled glass micropipette (diameter =  $\sim$ 80  $\mu$ m) that was connected and sealed to a 50  $\mu$ l syringe with hot melt glue (19). This allowed us to perform a single diminutive volume injection of contrast agents without significant injury to the dura mater and, thus, without CSF leakage. The micropipette was left in place for 1 additional minute to allow the wound to close. The intracisternal injection was conducted at a flow rate of 0.6  $\mu$ l/min over 6 min. About 28 min after the start of blood occlusion, the function of the glymphatic system and cerebral edema were evaluated by MRI.

### MRI Experiments and Imaging Analysis

Following surgery and cisterna magna injection, animals were transferred to an MRI-compatible cradle. About 1.5% isoflurane in oxygen was continuously delivered to the animal through a nose cone. The core body temperature of the mice was maintained at 37°C, and respiratory rate was maintained between 70 and 100 breaths per minute. Each MRI was acquired on an 11.7T Pharmascan MRI system (Bruker, Germany) equipped with surface coils. A baseline scan was acquired before intrathecal infusion of the paramagnetic contrast agent. 3D T1WI was then performed with a fast low angle shot sequence with parameters as follows: magnetic field strength = 11.75123799 Tesla, repetition time/echo time (TR/TE) 50/3.5 ms, field-of-view (FOV) = 16 mm  $\times$  16 mm, matrix = 128  $\times$  128, slice thickness (ST) = 0.3 mm, flip angle (FA) = 15°. 3D-TOF imaging was performed with the following parameters: TR/TE 12/2.0 ms, field-of-view (FOV) = 16 mm  $\times$  16 mm, matrix = 120  $\times$  120, ST = 0.13 mm, FA = 20°. T2-weighted (T2W) imaging was performed with the following parameters: TR/TE 2500/30 ms, FOV = 16 mm  $\times$  16 mm, matrix = 256  $\times$  256, ST = 0.5 mm, FA = 90°. Finally, diffusion-weighted imaging (DWI) was performed with parameters set as follows: TR/TE 3200/23 ms, FOV = 16 mm  $\times$  16 mm, matrix = 180  $\times$  180, ST = 0.3 mm, FA = 90°. The time course of distribution of the contrast agent throughout the brain was assessed as a measure of glymphatic flow, as demonstrated in a previous study (9, 22). The time-resolved T1W SI in the striatum, cortex, and cerebral ventricles were used to obtain the average hydrodynamic response curves. These time series were also used to illustrate the tissue uptake of BOPTA-Gd tracers over time. The ADC values were calculated automatically by the 11.7T Pharmascan MRI system and were displayed as a parametric map that indicated the degree of water molecule diffusion through different tissues.

Then, ADC measurements were acquired for a given region by drawing regions of interest (ROIs) on the ADC map (23).

### Triphenyl Tetrazolium Chloride (TTC) Staining

Animals were anesthetized and perfused with 20 ml of ice-cold saline. After immediate decapitation, the brains were extracted and sliced into six 1.5 mm coronal sections and immersed into 2% 2,3,5-triphenyl tetrazolium chloride (TTC) (Sigma-Aldrich) for 10 min at room temperature. Images were then acquired with a digital camera.

### Section Preparation

About 150 min after surgery, the deeply anesthetized pMCAO animals ( $n = 4$ ) and sham-operated animals ( $n = 4$ ) were sacrificed. All animals were then transcardially perfused with ice-cold saline, followed by 4% paraformaldehyde (PFA). Brains were removed, postfixed in PFA overnight at 4°C, dehydrated in the ascending alcohol series, rinsed by xylene, and embedded in paraffin blocks. Coronal sections (bregma +0.38 mm to +1.10 mm) were serially cut at 3  $\mu$ m thickness using a paraffin slicing machine (RM2135, Leica Microsystems, Germany).

### Immunofluorescence

After deparaffinization and hydration, antigen recovery was performed with ethylene diamine tetraacetic acid antigen retrieval buffer (pH 8.0). Coronal sections were maintained at a subboiling temperature for 8 min to facilitate staining with an AQP4 antibody. Sections were then blocked in phosphate-buffered saline (PBS) with 3% bovine serum albumin (BSA) for 30 min, and stained sequentially with primary mouse antibody AQP4 (1:500, #GB12529, Servicebio) and Alexa Fluor 594 antimouse (1:300, #GB21301, Servicebio), together with the fluorescein isothiocyanate (FITC) conjugate *Bandeiraea simplicifolia* Isolectin B4 (BSI-B4, 1:50, #L-2895, Sigma). The brain sections were then covered with an antifade medium containing 4',6-diamidino-2-phenylindole (DAPI, #D21490, Invitrogen). For this experimental step, IB4-FITC (2 mg dissolved in 2 ml saline, 0.05 mg per animal) was intravenously administered to the animals to identify the basement membrane. This was an important step as IB4 binds to a-D-galactose residues in the basement membrane secreted by endothelial cells (24). In each group, the circulation period of IB4-FITC was ensured for 180 min before sacrifice.

### Immunohistochemistry

After deparaffinization, hydration, and antigen retrieval, sections were washed and incubated with the 3% hydrogen peroxide (H<sub>2</sub>O<sub>2</sub>) at room temperature for 15 min to block endogenous peroxidase. Then tissues were washed and blocked with 3% BSA at room temperature for 30 min. Tissue sections were incubated with primary mouse antibody AQP4 (1:2,000, #GB12529, Servicebio) at 4°C overnight. Following PBS wash, sections were incubated with secondary antibody goat antimouse IgG (1:200, #GB23303, Servicebio) labeled with horseradish peroxidase, incubate at room temperature for 50 min. Then visualized with diaminobenzidine reagent (#G1211, Servicebio).

## Imaging Analysis

Microphotographs for analyzing immunofluorescence were captured by laser scanning confocal microscopy (FV1200, Olympus Microsystems, Japan) to generate 3-channel fluorescence images of the cerebral cortex and striatum. Images were obtained at 100× magnification and quantified using the ImageJ software (Bethesda, MD, USA). For immunofluorescent quantification of each antigen, at least three selected visual fields (bregma +0.38 to +1.10 mm) from each animal were imaged. Imaging parameters were constant throughout all imaging sessions. The background fluorescence for each channel was conformably subtracted and the perivascular expression of AQP4 was then measured after that in the soma (“depolarization”) was subtracted.

Microphotographs for analyzing immunohistochemistry were captured by conventional fluorescence microscopy (BX60, Olympus Microsystems, Japan). For the AQP4 examination, at least three high-power fields at 100× magnification were randomly selected and imaged for each animal. The ROI on the AQP4 display included the ependymal wall and a small amount of surrounding brain tissue in the bilateral brain of pMCAO animals. The average optical density (AOD) of AQP4 in each field was quantitatively calculated using the ImageJ software. All imaging parameters were constant throughout all imaging sessions.

## Quantification of AQP4 Expression and Polarization

To evaluate global and perivascular AQP4 expression levels, the mean AQP4 immunofluorescence intensity was measured within each visual field and the perivascular space. Evaluation of the polarization of AQP4 to perivascular end-feet was performed by measuring the immunofluorescence intensity of AQP4 immunoreactivity across sections of blood vessels labeled by IB4-FITC in each brain region studied. AQP4 polarization was measured by comparing the intensity ratios of AQP4 at perivascular domains vs. those in the parenchymal domains, as evaluated previously (25). The threshold was determined based on immunostained control slices.

## Statistical Analysis

Statistical analyses were conducted using Prism (GraphPad Software, V8.3.0, La Jolla, USA). The data are represented as mean ± SD. Either a repeated measure two-way ANOVA or a regular two-way ANOVA was used for regional comparisons, followed by Tukey’s multiple comparisons test. A one-way ANOVA was used for regional comparisons, and unpaired *t*-tests were used for single comparisons. Pearson correlation analysis was utilized to evaluate the link between edema and glymphatic failure. A *p*-value < 0.05 was considered statistically significant.

## RESULTS

### Occlusion of Blood Flow in pMCAO Mice

To study the dynamics of glymphatic flow following cerebral edema, we induced pMCAO (Figure 1A) in the left (L)

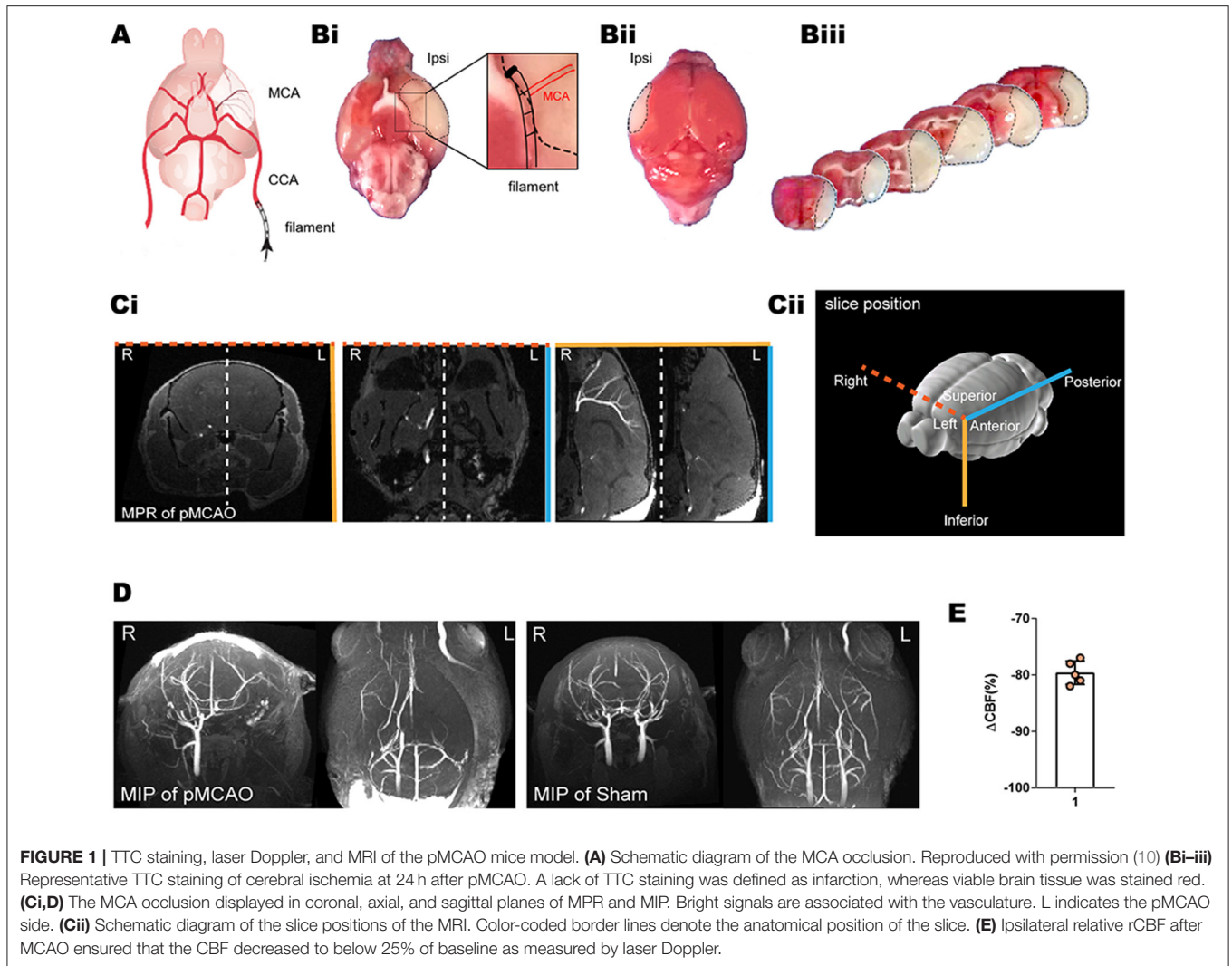
hemisphere of mice, examined ischemic regions using TTC staining 24 h after pMCAO (Figures 1Bi–iii). We confirmed the occlusion of MCA by multiplanar reconstructions (Figure 1C) and maximum intensity projections (Figure 1D) in 11.7 T MR images. In both images, pMCAO was represented by a unilateral loss of visible vasculature ipsilateral in the site of model induction. By contrast, bilateral vasculature could be observed in the sham-operated animals. The loss of vascular imaging markers was also quantified by calculating the CBF, as recorded by laser Doppler, to ensure that it was below 25% of baseline. pMCAO resulted in an immediate and strong reduction in the relative CBF (rCBF) ( $79.6\% \pm 2.1\%$ ; Figure 1E).

### In vivo Evaluation of Glymphatic Flow in Sham-Operated Mice

We then investigated the glymphatic flow in sham-operated mice by *in vivo* CEMRI with BOPTA-Gd injection (BOPTA-Gd+) in the cisterna magna (Figure 2C). Sequential multiplanar reformation or reconstruction images revealed that gadolinium progressively entered the brain parenchyma, as shown in the schematic diagram in Figure 2A. The schematic diagram of the approximate ROIs used for MRI quantification is indicated in Figure 2B. In these images, an increase in SI, representing contrast agent uptake, can be observed as a function of time. Overall, the routes of CSF distribution were consistent with previous reports (Figure 2C) (26). Meanwhile, the contrast agent sequentially flowed from the cisterna magna to the bilateral, third, and fourth cerebral ventricles, as shown in Figure 2C. At 70 min postinjection, the brain ROI were completely perfused with the tracers (Figure 2C). The average time evolution curves illustrate the dynamics of tissue uptake of BOPTA-Gd tracers (Figure 2D). We also detected extracerebral CSF drainage routes at 14 min after BOPTA-Gd injection. Tracers drained from the subarachnoid space alongside the cranial nerves, such as the cochleovestibular and optic nerves (Figure 2E).

### Glymphatic Transport Kinetics Malfunction in the Acute Phase of pMCAO Mice

Interestingly, in the MRI we noticed a blockage of the ipsilateral (L) parenchyma and the bilateral ventricle perfusion immediately after pMCAO (Figures 3A,Ci). By contrast, the inflow of contrast agent was observed in the contralateral (R) hemisphere in the pMCAO and the sham-operated animals, further suggesting that glymphatic flow was altered in this pMCAO mouse model. To quantify these effects, we calculated the corresponding SI in the cortex, striatum, and ventricles in the pMCAO and the sham-operated animals (Figures 3Bi,ii,Di,ii). We found that glymphatic perfusion of the ipsilateral cortex/striatum and bilateral cerebral ventricles of the pMCAO mice was reduced compared with sham-operated animals. By contrast, glymphatic perfusion in the contralateral cortex/striatum was increased. These results provide evidence of glymphatic perfusion from the cisterna magna to the cerebral ventricles. However, the volume of the ventricles (Figure 3Cii) was reduced in the ipsilateral pMCAO mice and was accompanied by a delayed influx in the



bilateral ventricles (**Figure 3D**). The schematic diagram of the anatomical position of ventricles, and the approximate ROIs used for MRI quantification of the lateral ventricle volume are shown in **Figure 3E**.

## Analysis of the Link Between Ischemic Edema and Glymphatic Failure

To evaluate cerebral edema, we acquired T1WI, DWI, and ADC brain maps, these sequential scans were performed 28 min after pMCAO with 14 min BOPTA-Gd injections until 178 min (150 + 28 min) ( $n = 3$  per group), serial acquisition of MR images was performed using an interval of about 12 min, and confirmed brain infarction by T2W images at ~178 min (**Figure 4A**). Accordingly, we acquired the T1W and ADC value brain maps sequentially in the sham-operation group 14 min after BOPTA-Gd injection. Glymphatic transport kinetics were determined based on the SI in T1WIs, while cytotoxic edema was identified as cases of DWI hyperintensity with reduced diffusion and with ADC dark signal (27). When we measured molecular motion with DWI, only the ADC value was calculated. We observed a

positive correlation between SI in T1WIs and the corresponding ADC value in the cortex, striatum, and periventricular zone, suggesting that the impaired glymphatic transport kinetics in these regions are associated with the progression of pMCAO edema, as indicated by ADC values changes (**Figures 4B–D**).

## Immunofluorescent Analysis of AQP4 Expression and Polarization

Representative images of pMCAO and sham-operated animals (**Figures 5A–C**) showed an ischemia-affected ipsilateral (L) cortex and striatum 150 min after surgery. The vascular endothelial surface was delineated by I-B4 staining. At 150 min after pMCAO induction, parenchymal vessels in pMCAO animals exhibited endothelial IB4-FITC signals that did not differ from those of sham-operated animals (**Figure 5B**). This lack of difference indicated that the BBB remained intact (18, 21). In the current work, AQP4 was conjugated with Alexa Fluor 594, and nuclei were visualized with DAPI. AQP4 polarization levels were obtained by comparing the expression ratio of AQP4 at perivascular domains vs. parenchymal domains (25),

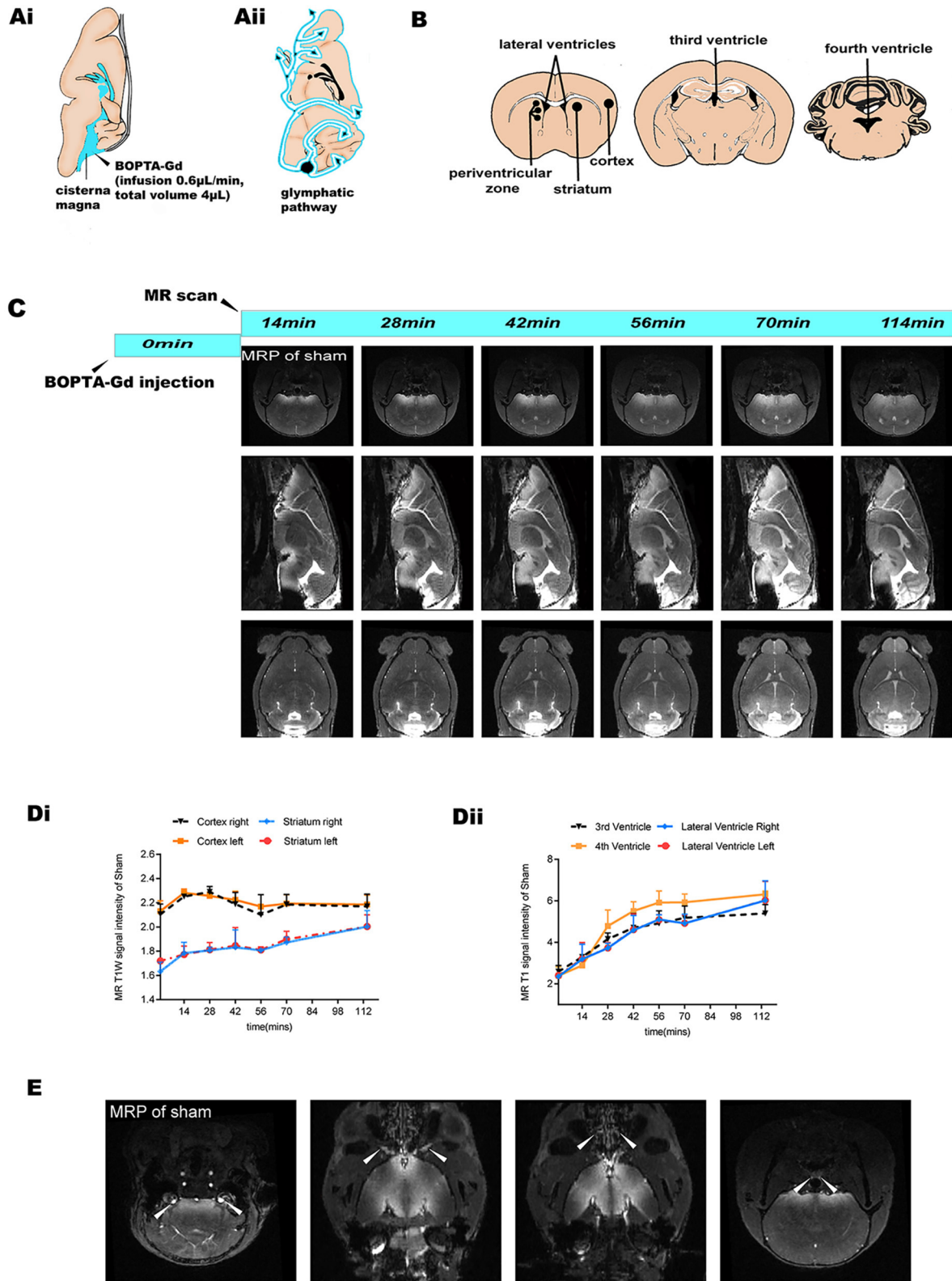
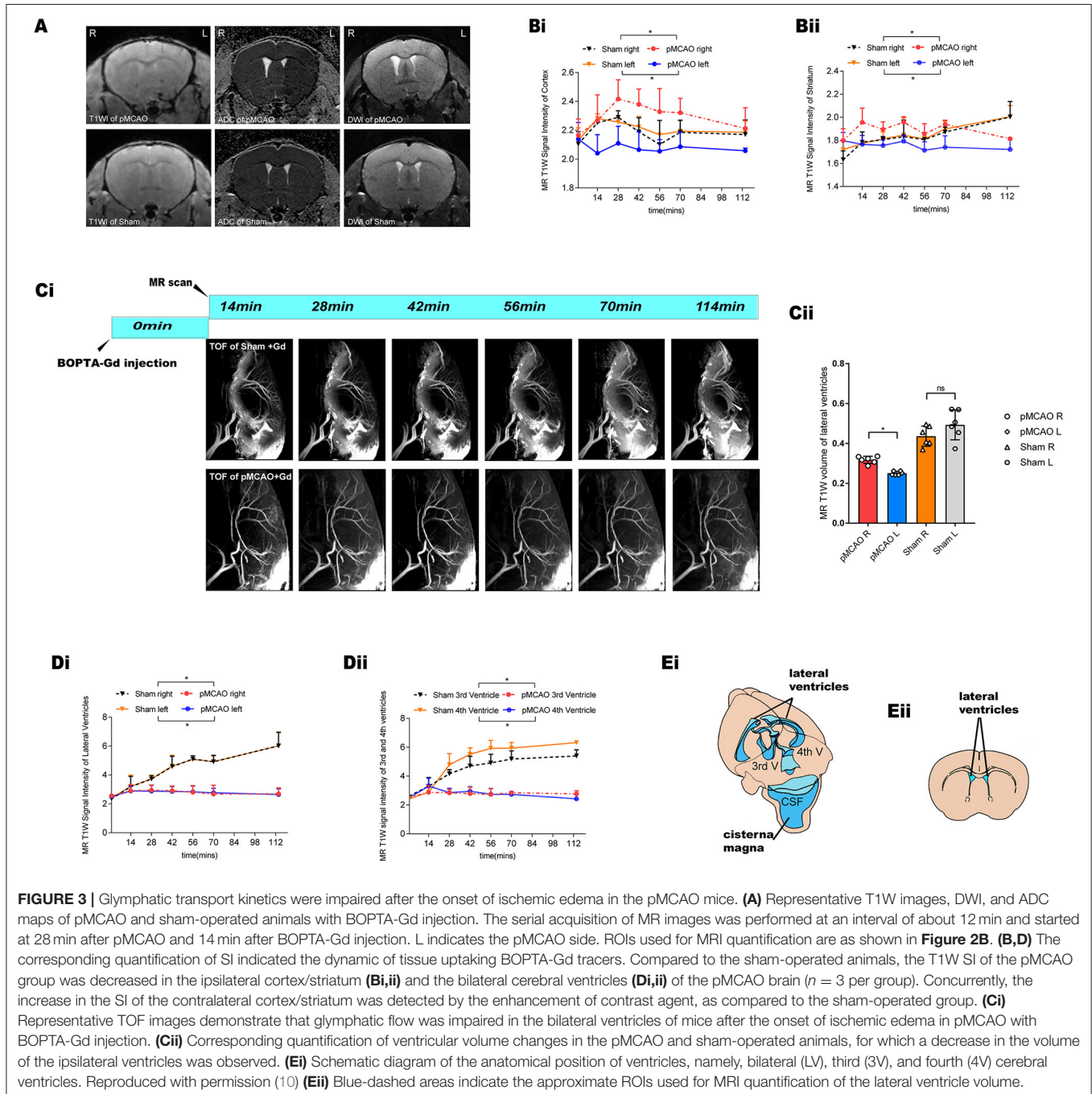


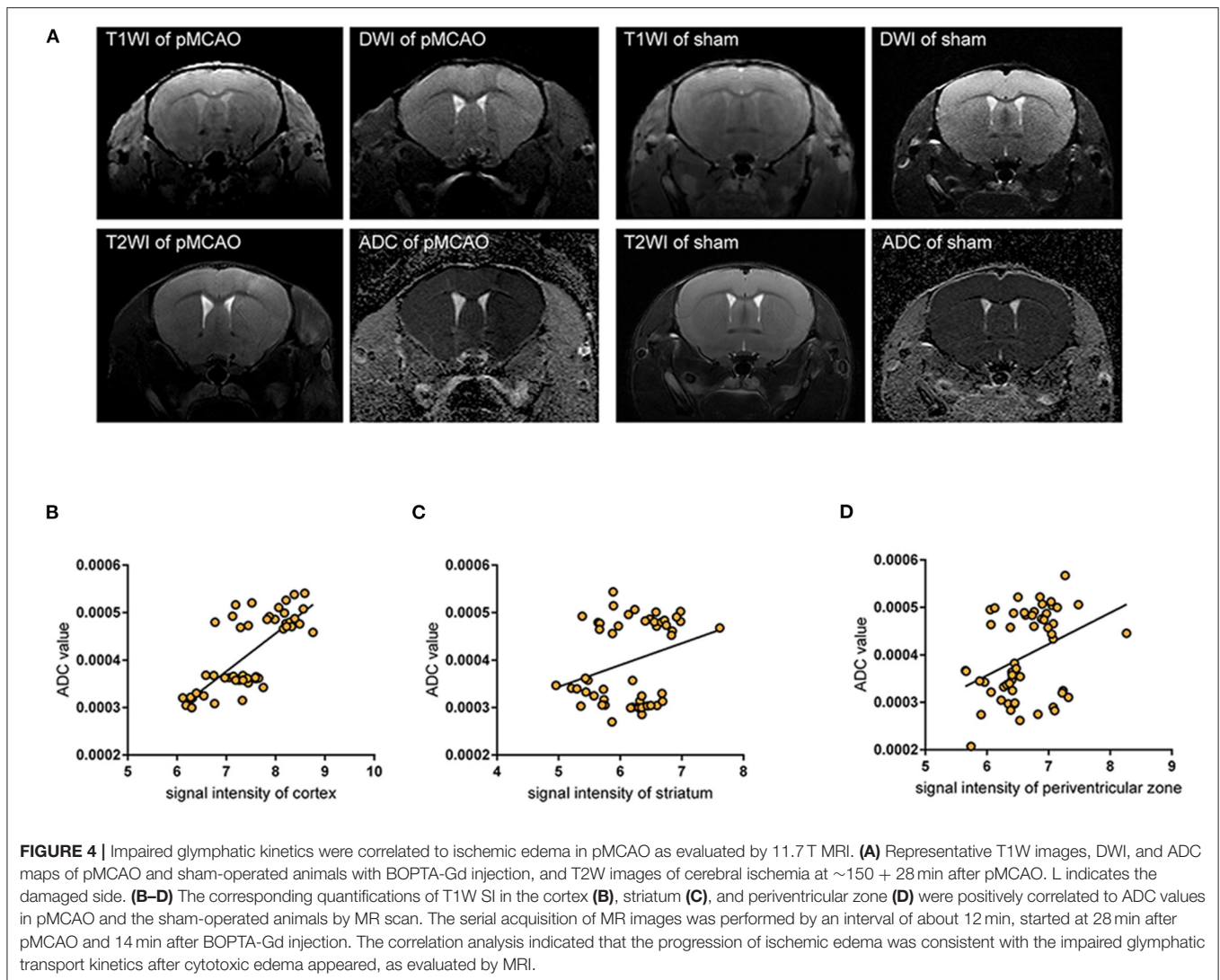
**FIGURE 2 |** MRI-based evaluation of glymphatic perfusion. **(Ai,ii)** Schematic diagram of cisterna magna injection and the CSF drainage routes from the cisterna magna (alongside cerebral ventricles and ventral brain surface). **(B)** Schematic diagram of the approximate ROIs used for MRI quantification of SI, including the striatum, cortex, periventricular zone, and bilateral, third, and fourth cerebral ventricles. **(C)** Representative coronal, sagittal, and axial slices of CEMRI MRP images (Continued)

**FIGURE 2** | from the sham-operated group (BOPTA-Gd+), showing progressive enhancement of the brain parenchyma and cerebral ventricles. **(Di,ii)** Corresponding quantification of the SI from the sham-operation striatum, cortex, and cerebral ventricles. The average time evolution curves illustrate the dynamic of tissue uptake of BOPTA-Gd tracers ( $n = 3$  per group). **(E)** Extracerebral CSF drainage routes revealed by the sham-operated group (BOPTA-Gd+). Arrows indicate cochleovestibular nerves, optic nerves, cribriform plate, and the peritracheal lymph nodes (from left to right, respectively).



which were analyzed on corresponding images obtained under  $100\times$  magnification. Specifically, we compared the contralateral tissue 150 min after surgery in pMCAO and sham-operated animals. Overall, in pMCAO animals, we found no significantly

altered global AQP4 expression (**Figure 5E**). Quantitative analysis showed that perivascular polarity of AQP4 decreased in ipsilateral pMCAO brains, with the most pronounced effects in the cortex and the striatum (**Figure 5D**). The



widespread loss of perivascular AQP4 polarization accompanied the decline in glymphatic dynamics. Representative image of immunofluorescent staining of PVS in the sham-operated group is shown in **Figure 5F**.

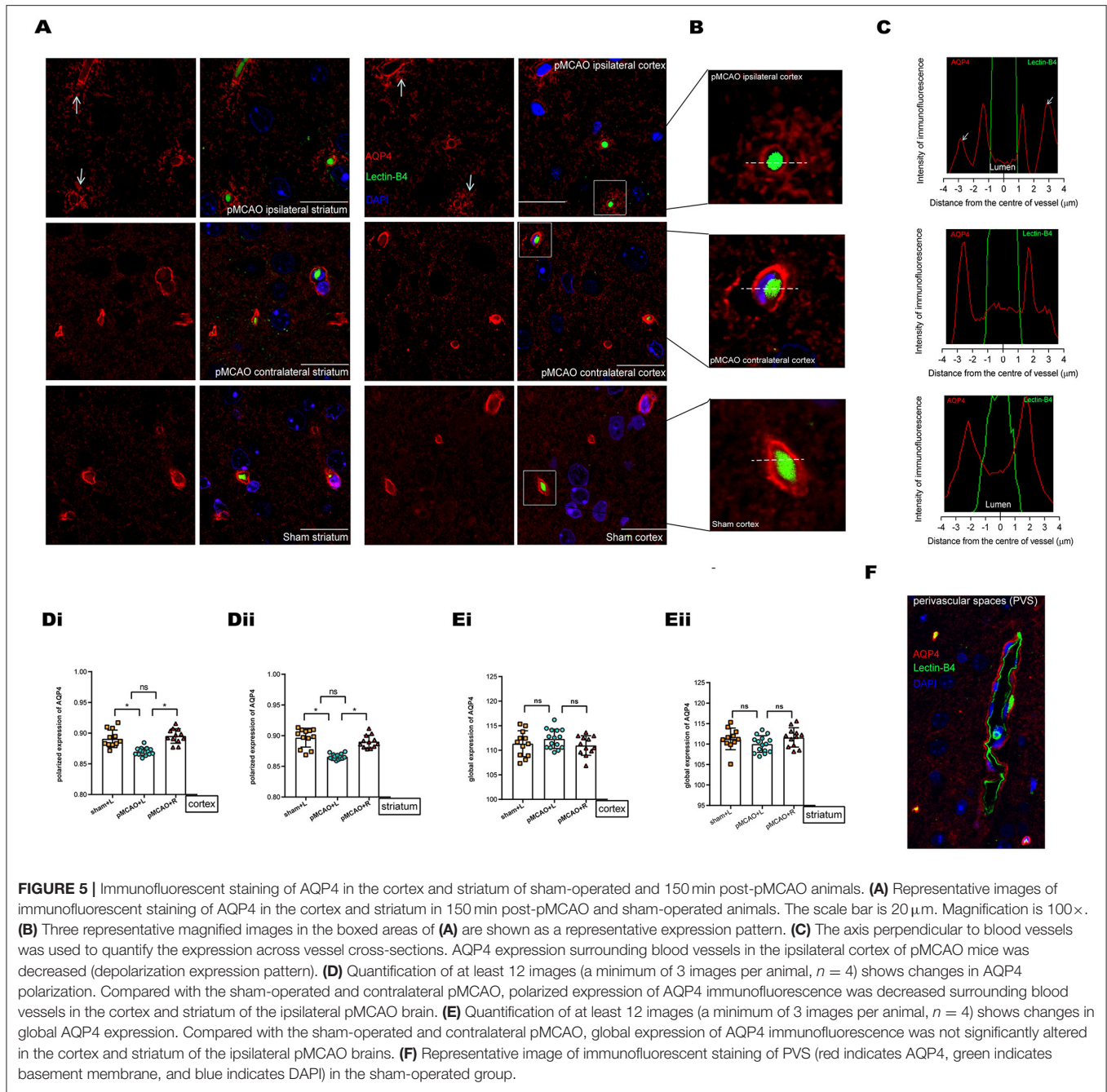
### Immunohistochemical Analysis of AQP4 Expression in the Ependymal Wall

Representative images showing AQP4 immunohistochemical staining (brown) of coronal brain sections in the lateral ventricle (LV) ependymal barrier (**Figures 6A,B**) revealed that AQP4 expression was decreased in the LV ependymal wall of the ipsilateral pMCAO brain (**Figure 6C**). These images also revealed AOD values with no apparent abnormalities in ependymal architecture. Furthermore, we observed a positive correlation between the corresponding ADC values in the periventricular zone of pMCAO animals at the MR scan acquired after 150 min and the AOD of AQP4 in the immunohistochemical staining of bilateral LV ependymal walls (**Figure 6D**). This result suggests that decreased expression of AQP4 in ependymal

walls was correlated to the diminishing of ADC values in the periventricular zone.

### DISCUSSION

Our results demonstrate in a pMCAO model with an intact BBB (18, 21) that the accumulation of edema is not accompanied by the transendothelial extravasation water (28) across the BBB. Of note, at as early as 150 min post-pMCAO, in the period during which the transformation of cytotoxic edema to vasogenic edema occurs, the ischemic edema regions showed a depolarization of AQP4 in the PVSs. The key finding was that there was a positive correlation between T1WI SI and the corresponding ADC values in the cortex, striatum, and periventricular zone. This suggested that glymphatic transport kinetics were impaired after the ischemic edema appeared in pMCAO, were accompanied by depolarization of AQP4, and were correlated to the progression of edema.



Cerebrospinal fluid (CSF) can provide a predominant source for the initial rise in the brain water content of ischemic tissues. The glymphatic influx of CSF into the PVSs (9) of ischemic brain tissues is the critical cause of acute ischemic brain edema within  $\sim$ 5 min (10). Given the possible treatment strategies require the time for the operation to be executed, it is necessary to investigate the specific contribution of the glymphatic dynamics in different stages of acute ischemia edema. As such, we investigated the pattern of glymphatic flow that could account for the liquid drainage in the parenchyma and periventricular zone following induced acute ischemic brain edema as a follow-up study. Uptake

of tracers and extracerebral CSF drainage routes have been observed in sham-operated animals as shown in **Figures 2C,E**. In the pMCAO model, we found that CSF dynamic flow was reduced in the ipsilateral brain parenchyma and accompanied by an increase in flow in the contralateral as indicated in **Figure 3**. These observations suggest that the accumulation of liquid in pMCAO brains may result from an impaired glymphatic system or be responsible for the suppression of the glymphatic dynamics. Glymphatic transport is driven by arterial pulsation (29, 30), and ISF drainage may be increased by vasomotion as a driving force, as observed by two-photon microscopy (31). Therefore, the

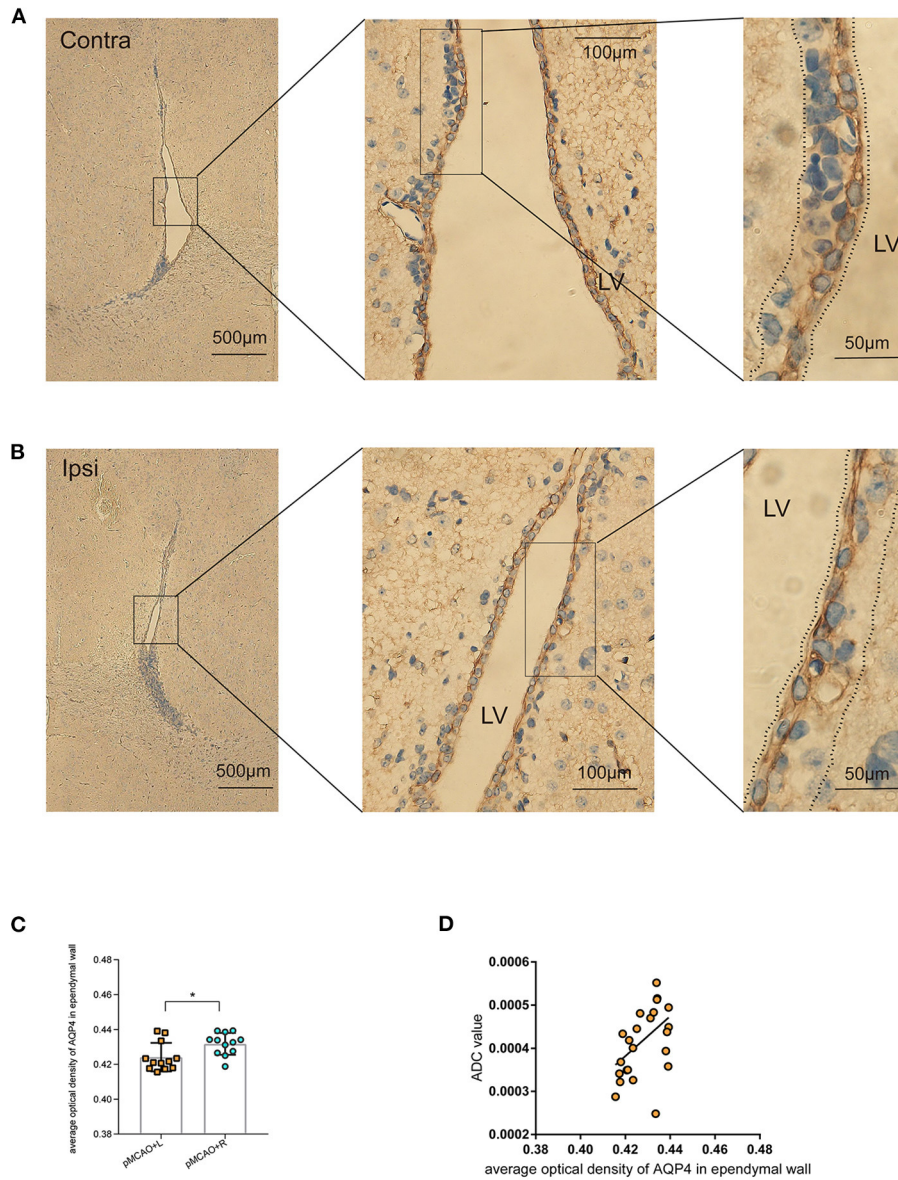


**FIGURE 6 |** Immunohistochemical staining of AQP4 in the LV ependymal wall of 150 min post-pMCAO animals. **(A,B)** Representative images showing AQP4 immunohistochemical staining (brown) of coronal brain sections in the LV ependymal barrier of the bilateral brain in 150 min post-pMCAO animals. These images revealed comparable morphology of the bilateral ependyma walls outlining LV. Boxed areas are enlarged successively from left to right. The areas between the dotted lines were used to quantify AQP4 expression in the LV ependymal wall. The scale bars are indicated in each box, and the magnification is 4 $\times$ , 40 $\times$ , and 100 $\times$ , respectively. **(C)** Quantification of at least 12 images (a minimum of three images per animal,  $n = 4$ ) revealed changes in AQP4 expression. Compared with the contralateral pMCAO animals, AOD of AQP4 immunohistochemical staining was reduced in the LV ependymal wall of the ipsilateral pMCAO brain. **(D)** The corresponding ADC values in the periventricular zone of pMCAO animals at the 150 min MR scan were positively correlated to the AOD of AQP4 in the immunohistochemical staining of bilateral LV ependymal walls. ROIs used for MRI quantification are as shown in **Figure 2B**.

regional differences in glymphatic flow observed here may be due to discrepancies in a convective flow drive mechanism. However, another study recently provided evidence that the directional movement of CSF in the PVS is not generated by arterial pulsations and can be explained by naturally occurring flow (32). Furthermore, contrast agents were found to rapidly enter the ventricular system in the sham-operated group (**Figure 3**),

suggesting that cistern-labeled CSF could enter the ventricles. Previous data suggest a critical role of the ventricle in brain water drainage (33, 34). PVS pathways were found to connect different parts of the brain to the ventricles. In particular, a connection between the lateral ventricle and ventral brain surface has been identified through PVS pathways surrounding the anterior choroidal artery (33). Thus, there might exist a pathway

that involves the transependymal exchange of CSF, followed by the clearance therefore from the parenchyma *via* a mechanism similar to the glymphatic system.

As a key determinant of the glymphatic system, AQP4 is a transmembrane and bidirectional water channel that is highly expressed on astrocytes, particularly at the sites of fluid transport at the pial surrounding cerebral blood vessels and ependymal surfaces in contact with the CSF in the ventricular system, and acts as a facilitator for water transport both in cells and tissues (16, 35–37). In a recent study, CSF was identified as a major source of water that drives directly AQP4-dependent edema, which acts as a consequence of CSF and brain ISF exchange (10). Other studies suggested a controversial opinion, in that the depletion of astrocytic AQP4 caused water to accumulate in the brain (34) and markedly impaired interstitial solute clearance (38). Moreover, recent studies on AQP4-knockout mice have suggested that the water movement in the paravascular space is mediated through diffusion and convective flow (39, 40), and elucidated the concept that AQP4 plays a vital role in the central nervous system (CNS) water homeostasis. In this sense, AQP4 is thought to facilitate the development or clearance of CNS edema. Previous studies have shown the glymphatic clearance function depends on the highly selective expression of AQP4 in microvascular end-feet of astrocytes in the aging brain, traumatic brain injury, and animal models of cerebral small vessel disease (38, 41, 42). We explored here the loss of polarized AQP4 expression leads to compromised glymphatic activity as soon as edema appeared at 150 min post-pMCAO (Figure 5). We also observed a decrease in AQP4 expression in the LV ependymal wall of the ipsilateral pMCAO brain, accompanied by a reduced volume of the ventricles and a delay in CSF uptake from the cisterna magna, as shown in Figures 3C, 6C. The participation of AQP4 in structural function, such as the distensibility capacity of the ventricular system, is also related to CSF homeostasis by altering the CSF drainage and the ventricular compliance in AQP4 mutation mice (43). Aquaporins (AQPs) line the periventricular wall. Previous studies have hypothesized that AQP4 participates in the development and integrity of the ependyma, however, the underlying mechanism of this effect has not been identified (44).

Cerebral edema is primarily an intracellular water accumulation process, caused by water influx through AQP4 passively in response to osmotic gradients (16), and usually as a consequence of ischemia-hypoxia. Of all the cell types susceptible to cytotoxic edema in the cerebral nervous system, astrocytes are particularly vulnerable (28). Along these lines, a recently proposed treatment targeting the mechanism of CNS edema is supported by the idea that AQP4 localization is also dynamically regulated at the subcellular level, from intracellular vesicles to the plasma membrane, affecting membrane water permeability (45). Due to the described dynamic subcellular changes of aquaporin abundance (45, 46), and there being highly polarized at the

fluid interface (15), the membrane permeability and either the influx of CSF or ISF dynamics must be selective or suppressed. AQPs have been validated as an important drug target but there is no single drug that has yet been approved to successfully target it, it is hard to target edema and the glymphatic function using one line of therapies (47, 48). The previous studies have shown an increased AQP4 membrane localization in primary human astrocytes which was not accompanied by a change in AQP4 protein expression levels (45, 46). This subcellular mislocalization can be a potential therapeutic target. More studies to investigate the communication between AQPs (mainly AQP4) and other therapeutic targets are required to identify AQP modulators. Targeting the ion channel function and regulation mechanisms of AQP4 subcellular relocalization provides new insights into drug development (49). Currently, chelation of  $Ca^{2+}$  or CaM inhibition through egtazic acid acetoxymethyl ester (EGTA-AM) (45) or trifluoperazine (TFP) (50) had been reported to effectively reduce ischemia CNS edema.

In conclusion, glymphatic transport kinetics were suppressed between the onset of cytotoxic edema and the disruption of the BBB. These impaired glymphatic transport kinetics were correlated to the diminishing of ADC values that vary depending on edema progression, as measured by MRI, and that are associated with the depolarization of AQP4 in both the parenchyma PVs and periventricular zone. As such, targeting the dynamic subcellular relocalization of the water channel protein AQP4, and improving glymphatic dynamics by promoting polarization of AQP4 may alleviate acute ischemic cerebral edema and similar pathologies.

## DATA AVAILABILITY STATEMENT

The raw data supporting the conclusions of this article will be made available by the authors, without undue reservation.

## ETHICS STATEMENT

The animal study was reviewed and approved by Huashan Hospital Institutional Review Board.

## AUTHOR CONTRIBUTIONS

JZ, WC, HW, HZ, YX, and GF performed the experiments, participated in data collection, and revision of this manuscript. WC, HW, and QD designed the study. HZ and YX analyzed the data. JZ drafted this manuscript and prepared figures. All authors contributed to the article and approved the submitted version.

## FUNDING

This study was supported by the National Nature Science Foundation of China (Nos. 81870915 and 82071197).

## REFERENCES

- Rosenberg GA. Ischemic brain edema. *Prog Cardiovasc Dis.* (1999) 42:209–16. doi: 10.1016/S0033-0620(99)70003-4
- Rocha M, Jovin TG. Fast versus slow progressors of infarct growth in large vessel occlusion stroke: clinical and research implications. *Stroke.* (2017) 48:2621–7. doi: 10.1161/STROKEAHA.117.017673
- Ferro D, Matias M, Neto J, Dias R, Moreira G, Petersen N, et al. Neutrophil-to-lymphocyte ratio predicts cerebral edema and clinical worsening early after reperfusion therapy in stroke. *Stroke.* (2021) 52:859–67. doi: 10.1161/STROKEAHA.120.032130
- Klatzo I. Pathophysiological aspects of brain edema. *Acta Neuropathol.* (1987) 72:236–9. doi: 10.1007/BF00691095
- Li Z, Li M, Shi SX, Yao N, Cheng X, Guo A, et al. Brain transforms natural killer cells that exacerbate brain edema after intracerebral hemorrhage. *J Exp Med.* (2020) 217:e20200213. doi: 10.1084/jem.20200213
- Dreier JP, Lemale CL, Kola V, Friedman A, Schoknecht K. Spreading depolarization is not an epiphenomenon but the principal mechanism of the cytotoxic edema in various gray matter structures of the brain during stroke. *Neuropharmacology.* (2018) 134:189–207. doi: 10.1016/j.neuropharm.2017.09.027
- Young W, Rappaport ZH, Chalif DJ, Flamm ES. Regional brain sodium, potassium, and water changes in the rat middle cerebral artery occlusion model of ischemia. *Stroke.* (1987) 18:751–9. doi: 10.1161/01.STR.18.4.751
- Simard JM, Kent TA, Chen M, Tarasov KV, Gerzanich V. Brain oedema in focal ischaemia: molecular pathophysiology and theoretical implications. *Lancet Neurol.* (2007) 6:258–68. doi: 10.1016/S1474-4422(07)70055-8
- Iliff JJ, Wang M, Liao Y, Plogg BA, Peng W, Gundersen GA, et al. A paravascular pathway facilitates CSF flow through the brain parenchyma and the clearance of interstitial solutes, including amyloid  $\beta$ . *Sci Transl Med.* (2012) 4:147ra111. doi: 10.1126/scitranslmed.3003748
- Mestre H, Du T, Sweeney AM, Liu G, Samson AJ, Peng W, et al. Cerebrospinal fluid influx drives acute ischemic tissue swelling. *Science.* (2020) 367:eaax7171. doi: 10.1126/science.aax7171
- Louveau A, Plog BA, Antila S, Alitalo K, Nedergaard M, Kipnis J. Understanding the functions and relationships of the glymphatic system and meningeal lymphatics. *J Clin Invest.* (2017) 127:3210–9. doi: 10.1172/JCI90603
- Lee S, Yoo RE, Choi SH, Oh SH, Ji S, Lee J, et al. Contrast-enhanced MRI T1 mapping for quantitative evaluation of putative dynamic glymphatic activity in the human brain in sleep-wake states. *Radiology.* (2021) 300:661–8. doi: 10.1148/radiol.2021203784
- Rasmussen MK, Mestre H, Nedergaard M. The glymphatic pathway in neurological disorders. *Lancet Neurol.* (2018) 17:1016–24. doi: 10.1016/S1474-4422(18)30318-1
- Alshuhri MS, Gallagher L, Work LM, Holmes WM. Direct imaging of glymphatic transport using H217O MRI. *JCI Insight.* (2021) 6:e141159. doi: 10.1172/jci.insight.141159
- Nielsen S, Nagelhus EA, Amiry-Moghaddam M, Bourque C, Agre P, Ottersen OP. Specialized membrane domains for water transport in glial cells: high-resolution immunogold cytochemistry of aquaporin-4 in rat brain. *J Neurosci.* (1997) 17:171–80. doi: 10.1523/JNEUROSCI.17-01-00171.1997
- Salman MM, Kitchen P, Halsey A, Wang MX, Tornroth-Horsefield S, Conner AC, et al. Emerging roles for dynamic aquaporin-4 subcellular relocalization in CNS water homeostasis. *Brain.* (2021). doi: 10.1093/brain/awab311
- Gaberel T, Gakuba C, Goulay R, Martinez De Lizarrondo S, Hanouz JL, Emery E, et al. Impaired glymphatic perfusion after strokes revealed by contrast-enhanced MRI: a new target for fibrinolysis? *Stroke.* (2014) 45:3092–6. doi: 10.1161/STROKEAHA.114.006617
- O'Donnell ME, Chen YJ, Lam TI, Taylor KC, Walton JH, Anderson SE. Intravenous HOE-642 reduces brain edema and Na uptake in the rat permanent middle cerebral artery occlusion model of stroke: evidence for participation of the blood-brain barrier Na/H exchanger. *J Cereb Blood Flow Metab.* (2013) 33:225–34. doi: 10.1038/jcbfm.2012.160
- Percie du Sert N, Hurst V, Ahluwalia A, Alam S, Avey MT, Baker M, et al. The ARRIVE guidelines 2.0: Updated guidelines for reporting animal research. *J Cereb Blood Flow Metab.* (2020) 40:1769–77. doi: 10.1177/0271678X20943823
- Engler-Chiurazzi EB, Brown CM, Povroznik JM, Simpkins JW. Estrogens as neuroprotectants: Estrogenic actions in the context of cognitive aging and brain injury. *Prog Neurobiol.* (2017) 157:188–211. doi: 10.1016/j.pneurobio.2015.12.008
- Krueger M, Mages B, Hobusch C, Michalski D. Endothelial edema precedes blood-brain barrier breakdown in early time points after experimental focal cerebral ischemia. *Acta Neuropathol Commun.* (2019) 7:17. doi: 10.1186/s40478-019-0671-0
- Iliff JJ, Lee H, Yu M, Feng T, Logan J, Nedergaard M, et al. Brain-wide pathway for waste clearance captured by contrast-enhanced MRI. *J Clin Invest.* (2013) 123:1299–309. doi: 10.1172/JCI67677
- El Kady RM, Choudhary AK, Tappouni R. Accuracy of apparent diffusion coefficient value measurement on PACS workstation: a comparative analysis. *AJR Am J Roentgenol.* (2011) 196:W280–284. doi: 10.2214/AJR.10.4706
- Peters BP, Goldstein IJ. The use of fluorescein-conjugated Bandeiraea simplicifolia B4-isolectin as a histochemical reagent for the detection of alpha-D-galactopyranosyl groups. Their occurrence in basement membranes. *Exp Cell Res.* (1979) 120:321–34. doi: 10.1016/0014-4827(79)90392-6
- Wang M, Iliff JJ, Liao Y, Chen MJ, Shinseki MS, Venkataraman A, et al. Cognitive deficits and delayed neuronal loss in a mouse model of multiple microinfarcts. *J Neurosci.* (2012) 32:17948–60. doi: 10.1523/JNEUROSCI.1860-12.2012
- Ramos M, Burdon Bechet N, Battistella R, Pavan C, Xavier ALR, Nedergaard M, et al. Cisterna magna injection in rats to study glymphatic function. *Methods Mol Biol.* (2019) 1938:97–104. doi: 10.1007/978-1-4939-9068-9\_7
- Gaddamanugu S, Shafaat O, Sotoudeh H, Sarrami AH, Rezaei A, Saadatpour Z, et al. Clinical applications of diffusion-weighted sequence in brain imaging: beyond stroke. *Neuroradiology.* (2022) 64:15–30. doi: 10.1007/s00234-021-02819-3
- Stokum JA, Gerzanich V, Simard JM. Molecular pathophysiology of cerebral edema. *J Cereb Blood Flow Metab.* (2016) 36:513–38. doi: 10.1177/0271678X15617172
- Iliff JJ, Wang M, Zeppenfeld DM, Venkataraman A, Plog BA, Liao Y, et al. Cerebral arterial pulsation drives paravascular CSF-interstitial fluid exchange in the murine brain. *J Neurosci.* (2013) 33:18190–9. doi: 10.1523/JNEUROSCI.1592-13.2013
- Mestre H, Tithof J, Du T, Song W, Peng W, Sweeney AM, et al. Flow of cerebrospinal fluid is driven by arterial pulsations and is reduced in hypertension. *Nat Commun.* (2018) 9:4878. doi: 10.1038/s41467-018-07318-3
- van Veluw SJ, Hou SS, Calvo-Rodriguez M, Arbel-Ornath M, Snyder AC, Frosch MP, et al. Vasomotion as a driving force for paravascular clearance in the awake mouse brain. *Neuron.* (2020) 105:549–61.e545. doi: 10.1016/j.neuron.2019.10.033
- Kedarasetti RT, Drew PJ, Costanzo F. Arterial pulsations drive oscillatory flow of CSF but not directional pumping. *Sci Rep.* (2020) 10:10102. doi: 10.1038/s41598-020-66887-w
- Magdoo KN, Brown A, Rey J, Mareci TH, King MA, Sarntinoranont M. MRI of whole rat brain perivascular network reveals role for ventricles in brain waste clearance. *Sci Rep.* (2019) 9:11480. doi: 10.1038/s41598-019-44938-1
- Vindedal GE, Thoren AE, Jensen V, Klungland A, Zhang Y, Holtzman MJ, et al. Removal of aquaporin-4 from glial and ependymal membranes causes brain water accumulation. *Mol Cell Neurosci.* (2016) 77:47–52. doi: 10.1016/j.mcn.2016.10.004
- Mestre H, Hablitz LM, Xavier AL, Feng W, Zou W, Pu T, et al. Aquaporin-4-dependent glymphatic solute transport in the rodent brain. *Elife.* (2018) 7. doi: 10.7554/eLife.40070.022
- Mamtilahun M, Tang G, Zhang Z, Wang Y, Tang Y, Yang GY. Targeting water in the brain: role of aquaporin-4 in ischemic brain edema. *Curr Drug Targets.* (2019) 20:748–55. doi: 10.2174/1389450120666190214115309
- Buffoli B. Aquaporin biology and nervous system. *Curr Neuropharmacol.* (2010) 8:97–104. doi: 10.2174/157015910791233204
- Kress BT, Iliff JJ, Xia M, Wang M, Wei HS, Zeppenfeld D, et al. Impairment of paravascular clearance pathways in the aging brain. *Ann Neurol.* (2014) 76:845–61. doi: 10.1002/ana.24271

39. Smith AJ, Yao X, Dix JA, Jin BJ, Verkman AS. Test of the 'glymphatic' hypothesis demonstrates diffusive and aquaporin-4-independent solute transport in rodent brain parenchyma. *Elife*. (2017) 6. doi: 10.7554/eLife.27679.019
40. Ray L, Iliff JJ, Heys JJ. Analysis of convective and diffusive transport in the brain interstitium. *Fluids Barriers CNS*. (2019) 16:6. doi: 10.1186/s12987-019-0126-9
41. Ren Z, Iliff JJ, Yang L, Yang J, Chen X, Chen MJ, et al. 'Hit & Run' model of closed-skull traumatic brain injury (TBI) reveals complex patterns of post-traumatic AQP4 dysregulation. *J Cereb Blood Flow Metab*. (2013) 33:834–45. doi: 10.1038/jcbfm.2013.30
42. Xue Y, Liu N, Zhang M, Ren X, Tang J, Fu J. Concomitant enlargement of perivascular spaces and decrease in glymphatic transport in an animal model of cerebral small vessel disease. *Brain Res Bull*. (2020) 161:78–83. doi: 10.1016/j.brainresbull.2020.04.008
43. Trillo-Contreras JL, Toledo-Aral JJ, Echevarría M, Villadiego J. AQP1 and AQP4 Contribution to Cerebrospinal Fluid Homeostasis. *Cells*. (2019) 8:197. doi: 10.3390/cells8020197
44. Li X, Kong H, Wu W, Xiao M, Sun X, Hu G. Aquaporin-4 maintains ependymal integrity in adult mice. *Neuroscience*. (2009) 162:67–77. doi: 10.1016/j.neuroscience.2009.04.044
45. Kitchen P, Salman MM, Halsey AM, Clarke-Bland C, MacDonald JA, Ishida H, et al. Targeting aquaporin-4 subcellular localization to treat central nervous system edema. *Cell*. (2020) 181:784–99. doi: 10.1016/j.cell.2020.03.037
46. Salman MM, Kitchen P, Woodroffe MN, Brown JE, Bill RM, Conner AC, et al. Hypothermia increases aquaporin 4 (AQP4) plasma membrane abundance in human primary cortical astrocytes via a calcium/transient receptor potential vanilloid 4 (TRPV4)- and calmodulin-mediated mechanism. *Eur J Neurosci*. (2017) 46:2542–7. doi: 10.1111/ejn.13723
47. Verkman AS, Anderson MO, Papadopoulos MC. Aquaporins: important but elusive drug targets. *Nat Rev Drug Discov*. (2014) 13:259–77. doi: 10.1038/nrd4226
48. Abir-Awan M, Kitchen P, Salman MM, Conner MT, Conner AC, Bill RM. Inhibitors of Mammalian Aquaporin Water Channels. *Int J Mol Sci*. (2019) 20:1589. doi: 10.3390/ijms20071589
49. Salman MM, Kitchen P, Yool AJ, Bill RM. Recent breakthroughs and future directions in drugging aquaporins. *Trends Pharmacol Sci*. (2022) 43:30–42. doi: 10.1016/j.tips.2021.10.009
50. Sylvain NJ, Salman MM, Pushie MJ, Hou H, Meher V, Herlo R, et al. The effects of trifluoperazine on brain edema, aquaporin-4 expression and metabolic markers during the acute phase of stroke using photothrombotic mouse model. *Biochim Biophys Acta Biomembr*. (2021) 1863:183573. doi: 10.1016/j.bbamem.2021.183573

**Conflict of Interest:** The authors declare that the research was conducted in the absence of any commercial or financial relationships that could be construed as a potential conflict of interest.

**Publisher's Note:** All claims expressed in this article are solely those of the authors and do not necessarily represent those of their affiliated organizations, or those of the publisher, the editors and the reviewers. Any product that may be evaluated in this article, or claim that may be made by its manufacturer, is not guaranteed or endorsed by the publisher.

Copyright © 2022 Zhang, Zhao, Xue, Liu, Fan, Wang, Dong and Cao. This is an open-access article distributed under the terms of the Creative Commons Attribution License (CC BY). The use, distribution or reproduction in other forums is permitted, provided the original author(s) and the copyright owner(s) are credited and that the original publication in this journal is cited, in accordance with accepted academic practice. No use, distribution or reproduction is permitted which does not comply with these terms.